

Compound eye inspired flat lensless imaging with spatially-coded Voronoi-Fresnel phase

Qiang Fu^{1,*}, Dong-Ming Yan^{2,3}, and Wolfgang Heidrich^{1,*}

¹King Abdullah University of Science and Technology, Thuwal, 23955-6900, Saudi Arabia

²National Laboratory of Pattern Recognition (NLPR), Institute of Automation, Chinese Academy of Sciences, 100190, Beijing, China

³School of AI, University of Chinese Academy of Sciences, China

*Corresponding authors: qiang.fu@kaust.edu.sa, wolfgang.heidrich@kaust.edu.sa.

ABSTRACT

Lensless cameras are a class of imaging devices that shrink the physical dimensions to the very close vicinity of the image sensor by integrating flat optics and computational algorithms. Here we report a flat lensless camera with spatially-coded Voronoi-Fresnel phase, partly inspired by biological apposition compound eye, to achieve superior image quality. We propose a design principle of maximizing the information in optics to facilitate the computational reconstruction. By introducing a Fourier domain metric, Modulation Transfer Function volume (MTFv), we devise an optimization framework to guide the optimal design of the optical element. The resulting Voronoi-Fresnel phase features an irregular array of quasi-Centroidal Voronoi cells containing a base first-order Fresnel phase function. We demonstrate and verify the imaging performance with a prototype Voronoi-Fresnel lensless camera on a 1.6-megapixel image sensor in various illumination conditions. The proposed design could benefit the development of compact imaging systems working in extreme physical conditions.

Introduction

Imaging devices, such as photographic objectives and microscopes, have long been relying on lenses to focus light and create a projection of the scene onto photosensitive sensors. In such designs, as in human eyes, the focal length of the lens presents a fundamental limit for the overall device form factor, and in particular rules out flat systems. In addition, various optical aberrations preclude the use of single lenses for wide field-of-view (FOV) imaging. Instead, groups of compound lenses that are carefully designed must be used for good image quality.

In nature, compound eyes present an alternative and ubiquitous vision system, found for example in insects^{1,2}. Figure 1a shows the microscopic structure of the compound eyes of an Australian ant, *Iridomyrmex purpureus*. Its vision system, known as apposition compound eyes³, is composed of an array of ommatidia, each of which includes a microlens, a crystalline cone, and a rhabdom. Such miniature architectures are intriguing for various solutions to compact imaging systems.

With the ever increasing demand for compactness of imaging optics, great efforts have been motivated to develop lensless cameras during the past few years. To date two prevailing lensless methods exist, natural compound-eye mimicry and heuristic point spread function (PSF) engineering. Analogous to insect compound eyes, various artificial eyes^{4,5} have been proposed to directly mimic the lenslet structures. These cameras are engineered on sophisticated curved surfaces to achieve wide FOV, high motion acuity, and large depth of field. The other strategy considers the entire system from the perspective of the PSF it generates^{6–10}. Instead of mapping each scene point to a single focus spot on the image plane, as in conventional lens-based systems, such lensless cameras render each scene point as a distributed pattern that covers large areas of the image plane. The captured raw data is meaningless to human eyes, but can be interpreted by computational imaging algorithms to reconstruct the latent image. However, neither the compound-eye mimicry nor PSF engineering offers a unified solution to optimal imaging performance, since the heuristic designs are not optimal according to any objective criterion.

Here we report a lensless camera with spatially-coded Voronoi-Fresnel phase to overcome the above limitations from a fundamentally distinct perspective. Inspired by the random and uniform distribution of lenslets in the apposition compound eyes (Fig. 1a), and motivated by an observation from the properties of the engineered heuristic PSFs⁸, we find that the image quality after algorithmic reconstruction is positively related to the sparse distribution of high-contrast bright spots in the PSFs, subject to the phase being physically realizable. In other words, lensless cameras favor PSFs with concentrated sparse patterns. From the perspective of information theory, Modulation

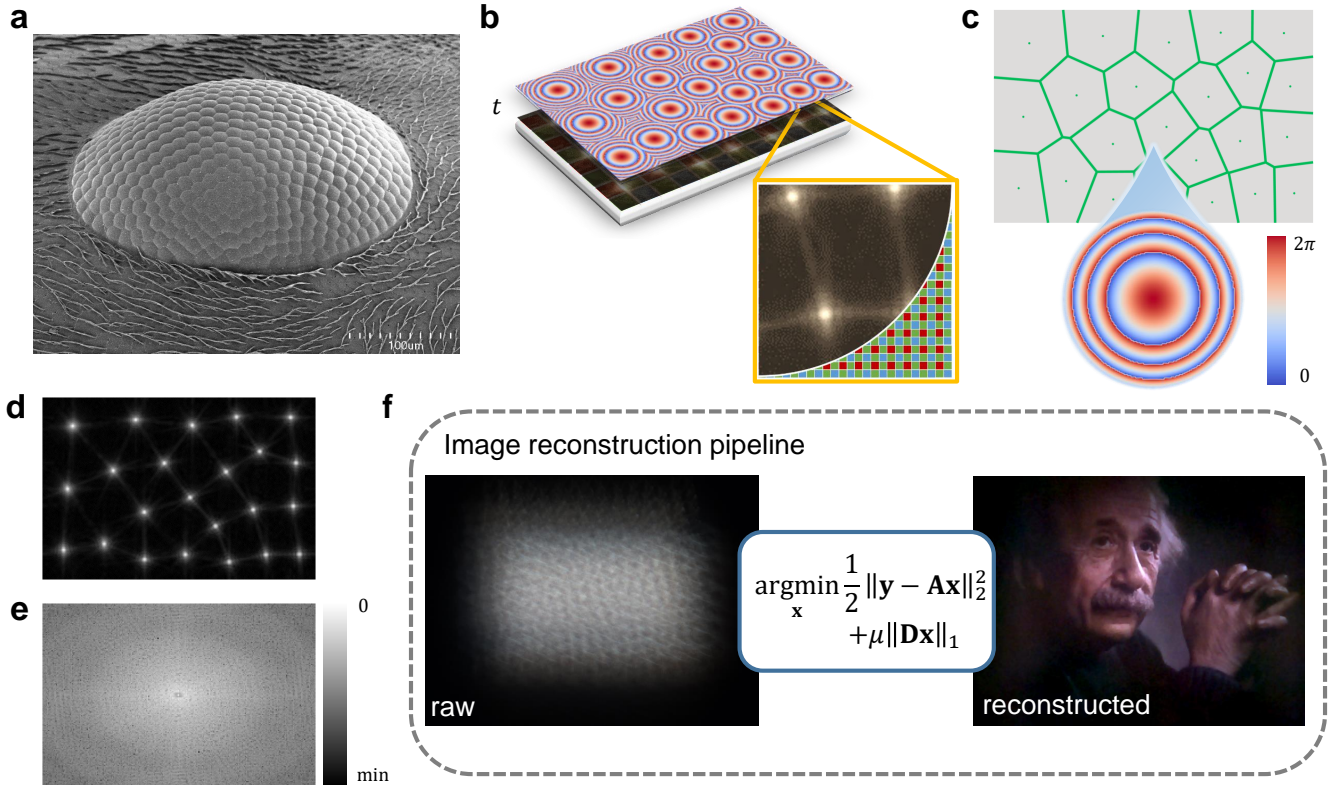


Fig. 1. Overview of Voronoi-Fresnel lensless imaging. **a** Micrograph of the compound eyes of an *Iridomyrmex purpureus* (image courtesy of Roberto Keller, ANTWEB1008536, from www.antweb.org). **b** The proposed Voronoi-Fresnel lensless camera consists only of a phase element in close proximity to an image sensor (the distance t is a few millimeters). The zoom-in illustrates the detailed PSF and Bayer filters. **c** The first-order Fresnel phase function is the building block of the camera and their center locations are distributed in a quasi-Centroidal Voronoi Tessellation across the 2D plane. **d** The PSF is an array of diffraction limited spots with optimal spatial locations. Intensity is in square root scale for better visualization. **e** MTF (in log scale) is uniform across the Fourier domain. **f** The image reconstruction pipeline converts the uninterpretable raw data (left) to a high quality image (right).

Transfer Function (MTF)¹¹, the Fourier counterpart of PSF, offers a more comprehensive measure to quantify this phenomenon. High frequency details are better recoverable in the reconstruction algorithms if the cut-off frequency is kept as large as possible, as well as the MTF is uniformly distributed in all directions in the Fourier domain. However, MTF is a 2D function of spatial frequencies. We therefore define MTF volume (MTFv) as a single-number metric for information maximization. A larger MTFv value encourages the system to transmit more information from hardware to software.

By applying this principle, we find that a set of individual point PSFs generated from the facet lenses in compound eyes makes an excellent match to the preferred PSFs in lensless imaging. To this end it is possible to engineer the optimal PSFs from a compound-eye mimicry. We devise a metric-guided optimization framework with modified Lloyd's iterations to find non-trivial and non-heuristic solutions to the problem. The resulting Voronoi-Fresnel phase features an irregular array of quasi-Centroidal Voronoi cells containing a base first-order Fresnel phase function (Fig. 1b). On the one hand, a first-order Fresnel phase function has proven to be efficient in concentrating light into a diffraction-limited spot in the paraxial region. On the other hand, blue-noise sampling generates randomized uniform distributions that preserve high-frequency information¹². Therefore, we choose to use the first-order Fresnel phase function as a building block and distribute their center locations across the available sensor. The resulting PSF is an array of diffraction limited spots with optimal spatial locations, but does not work individually as in conventional lenslet arrays. Instead, the entire PSF is coupled with computational algorithms to reconstruct sharp images. With significant lower requirement in optics and more flexibility in computation, the proposed method could benefit the development of imaging devices working in extreme physical conditions, such as portable microscopes,

wearable cameras, capsule endoscopy and so on. Unconventional imaging applications in various disciplines are expected to be triggered owing to the emerging importance of flat optics imaging.

Results

Voronoi-Fresnel phase

The overview of the proposed Voronoi-Fresnel lensless camera is illustrated in Fig. 1. By applying the proposed design principle, our Voronoi-Fresnel phase can generate optimal PSF (Fig. 1d) and MTF (Fig. 1e). An image reconstruction pipeline shown in Fig. 1f is then employed to recover high-quality images from the raw data that is not interpretable to the human eyes.

Analogous to the insect compound eyes, our Voronoi-Fresnel phase is composed of a base first-order Fresnel phase that is duplicated in various sub-regions on the 2D plane (Fig. 1c). The base Fresnel phase at the design wavelength λ is $\Phi_F(\xi, \eta, \lambda) = \exp[-jk(\xi^2 + \eta^2)/(2z)]$, where (ξ, η) are the Cartesian coordinates on the phase element plane, $k = 2\pi/\lambda$ is the wave number, and z is the distance from the optics to the image sensor. This phase function is a first-order approximation of a lens, thus produces a diffraction limited spot in the paraxial region.

We divide the design space into a number of adjacent regions that form a complete tessellation of the whole area. A typical tessellation is called a Voronoi diagram, which is a collection of sub-regions that contain points closer to the corresponding generating sites than any other sites. Each sub-region, also known as a Voronoi cell V_i , features a center location and a few vertices. The origin of the Fresnel phase function coincides with the center location, and the polygon determined by the vertices creates a distinct aperture for that cell. We refer to each Voronoi cell with the Fresnel phase as a Voronoi-Fresnel cell. The entire Voronoi-Fresnel phase is a collection of all the constituent Voronoi-Fresnel cells,

$$\Phi(\xi, \eta, \lambda) = \sum_{i=1}^K A_i(\xi - \xi_i, \eta - \eta_i) \cdot \exp\left(-j \frac{2\pi}{\lambda} \cdot \frac{(\xi - \xi_i)^2 + (\eta - \eta_i)^2}{2z}\right), \quad (1)$$

where $(\xi_i, \eta_i), i = 1, 2, \dots, K$ are the center locations of all the K Voronoi-Fresnel cells. The aperture function A_i is defined by the vertices of the i -th sub-region, where $A_i = 1$ inside V_i , and $A_i = 0$ outside. The union of all cells is the whole region, and any two different cells have no intersections. Thereby, all the Voronoi cells are independent, and there is no overlapping or gap between adjacent cells by definition.

PSF and the MTFv metric

The point spread function is characterized by the Fresnel diffraction pattern of the Voronoi-Fresnel phase on the image sensor. We assume incoherent illumination, so the PSF is the squared magnitude of the diffracted optical field. Since each Voronoi-Fresnel cell is independent, and is a shifted version from the origin to (ξ_i, η_i) , the panchromatic PSF is a union of individual PSFs integrated over the effective spectral range $[\lambda_1, \lambda_2]$,

$$\mathbf{PSF}(x, y) = \sum_{i=1}^K \int_{\lambda_1}^{\lambda_2} \mathbf{PSF}_i^0(x - \xi_i, y - \eta_i, \lambda) d\lambda, \quad (2)$$

where we denote $\mathbf{PSF}_i^0(x, y, \lambda)$ as the centered PSF as if the aperture were located at the origin of the design space. See Methods and Supplementary Note 1 for detailed derivations.

These individual apertures are significant, since the resulting diffraction pattern generates a small directional filter depending on the geometry. A collection of the distinct directional filters are resulted from different Voronoi cells. We investigate the directional filtering effect in Fig. 2. The center of a base Fresnel phase is first shifted randomly off the origin. A polygon aperture is then imposed on the phase profile. Here we evaluate four simple polygons, a triangle, a square, a pentagon, and a hexagon, as shown in Fig. 2a. The corresponding PSFs (brightness enhanced for better visualization) are rendered according to the color response function of an arbitrary color camera, as shown in Fig. 2b. Long tails in the PSFs show up in the perpendicular directions to the polygon edges due to diffraction.

It is more effective to evaluate the PSF through its frequency counterpart, the MTF. With higher MTF across all spatial frequencies, the imaging system preserves more details in the scene, a property that has long been used to evaluate the quality of lens-based optics. It can be seen from the log-scale panchromatic MTFs in Fig. 2c that the long tails in the spatial domain cause the MTF to drop in certain directions in the Fourier domain, while information is maintained in other directions. As the polygon becomes more regular in all edges, the directional filtering tends to be more isotropic. A circular aperture as in conventional lenses would result in no directional filtering effect at all.

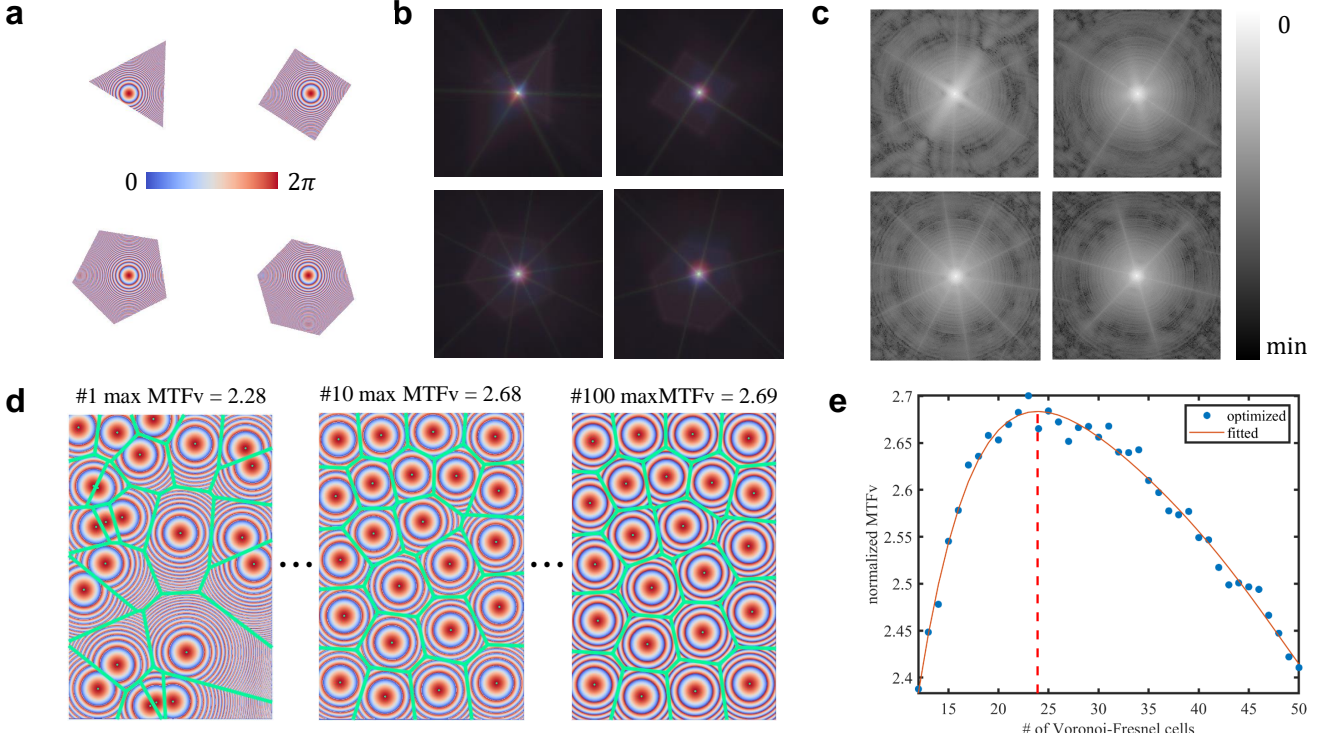


Fig. 2. Optimization of Voronoi-Fresnel phase. **a** Base Fresnel phase with various aperture geometries. Top: triangle and square. Bottom: pentagon and hexagon. The corresponding PSFs in **b** and MTFs in **c** show distinct directional filtering effects. PSFs are shown in the cubic root scale rendered in RGB color channels according to the color response functions of a color camera, and MTFs are shown in log scale for better visualization. **d** Given a fixed number of Voronoi-Fresnel cells $K = 23$, as the optimization evolves, the initial (left, Iteration #1) random distribution of Voronoi-Fresnel cells gradually tends to be more uniform (middle, Iteration #10) while keeping individual irregular apertures. The corresponding MTFv values increase until convergence (right, Iteration #100). **e** After the second step of parameter sweep on K , a plot of MTFv with respect to K can be fitted to a polynomial to find the optimal number of $K = 23$ in this example.

The distribution of the panchromatic PSF, or equivalently the MTF, is key to the imaging performance. However, MTF is a 2D function in the Fourier domain. It is difficult to use directly as a metric to optimize the optical element. We propose to use normalized panchromatic MTF volume (MTFv) as a single-number metric to evaluate the system performance. MTFv is defined as

$$\text{MTFv} = \frac{1}{|\Omega|} \iiint \text{MTF}(f_X, f_Y, \lambda) df_X df_Y d\lambda, \quad (3)$$

where f_X and f_Y are the Fourier frequencies, and $|\Omega|$ is the area of the design space. The spectral MTF is the Fourier transform of the spectral PSF, i.e., $\text{MTF}(f_X, f_Y, \lambda) = \mathcal{F}\{\text{PSF}(x, y, \lambda)\}$, with $\mathcal{F}\{\cdot\}$ being the Fourier transform. Essentially a larger MTFv value encourages more information to be recorded by the optical system, so we can employ it as a guide to seek for optimal PSFs generated by the Voronoi-Fresnel phase.

However, MTFv is a highly nonlinear and non-convex function of the number of Voronoi regions K and their center locations (ξ_i, η_i) . It is challenging to optimize the MTFv over the entire parameter space. Therefore, we do not aim at finding a closed-form solution to maximizing MTFv. Instead, we devise an optimization framework to search for a feasible solution. We show in Supplementary Note 2 that the effective MTF largely depends on three factors, the diffraction by each aperture; the phase delay terms in the Fourier domain that are introduced by the amount of spatial shifts from the centered PSFs; and the total number of the Voronoi-Fresnel cells K . The smallest dimension in the aperture geometry plays an important role due to diffraction. The phase delay terms would vary dramatically as the distances between each pair of center locations change. The optimal number of Voronoi-Fresnel cells is determined by a parameter sweep of K to find the best value.

Optimization and properties

Given a certain number of sites K within a fixed area, there are infinite Voronoi tessellations, whereas the MTFv values vary significantly. The number of sites K is also an important factor that affects the optimal MTFv. For example, taking the extreme case of $K = 1$, we get a compact single spot PSF, but it is impractical to realize such an optical element that covers the whole image sensor. On the other hand, when K approaches infinity, the PSF becomes pixel-wise uniform, and carries no useful information. Therefore, there exists an optimal number K that maximizes the MTFv.

In sampling theories, blue-noise sampling^{12,13}, among other sampling methods, has demonstrated its ability to generate randomized uniform distributions with no concentrated spikes in energy. This property shares similarities with the requirement for the distributions of Voronoi-Fresnel center locations. An effective way to achieve blue-noise sampling is by Centroidal Voronoi Tessellation (CVT)¹⁴. CVT is a special Voronoi diagram where the sites coincide with the mass centroids of the corresponding Voronoi regions (see Supplementary Note 3). CVTs give rise to cells in a close near-hexagonal packing, whose centroids follow a blue noise distribution. For this reason, they can be observed in many biological imaging systems, for example in the distribution of cones in the human retina¹⁵ or in the arrangement of ommatidia in compound eyes^{16,17} (cf. Fig. 1a). There are various algorithms to generate optimal CVT^{14,18}. A classic method uses Lloyd iterations¹⁹ to repetitively update the Voronoi sites with their centroids. However, a converged CVT might not necessarily be optimal in MTFv, because the directional filtering effect of individual PSFs is another factor that is not considered in CVT. It is necessary to devise a quasi-CVT algorithm to maximize MTFv with a similar Lloyd strategy.

To take the above factors into account, our optimization framework employs a two-step search scheme. In the first step, we fix the number of Voronoi sites K and initialize a set of K random coordinates. A Voronoi tessellation is constructed to produce the Voronoi-Fresnel phase function by Eq. (1). The corresponding MTFv metric is computed by Eq. (3). In each iteration, we compute the centroids of each cell and update the center coordinates with the centroids. A new Voronoi tessellation is constructed, leading to a new MTFv for the updated Voronoi-Fresnel phase. The new site coordinates and the corresponding MTFv are recorded only if the current MTFv is larger than the existing maximum MTFv, otherwise would be discarded. After each iteration, we compute the root-mean-square (RMS) distance between the new sites and the previous sites as the residual error. The iterations terminate when the residual error is smaller than a preset tolerance. In practice, the tolerance can be chosen as a fraction of the fabrication resolution, e.g., a tenth of the minimum manufacturable resolution would be a good choice. Smaller tolerances make little sense because the fabrication and alignment error would ruin the extra efforts. In the second step, we perform a parameter sweep for K to find the best number of sites. See Methods for more detailed descriptions.

An exemplary quasi-CVT optimization is shown in Fig. 2d followed by a parameter sweep step in Fig. 2e. This simulation uses 240×160 sensor pixels with a pixel pitch of $3.45 \mu\text{m}$. The distance is 2 mm from the optical plane to the sensor plane. The quasi-CVT optimization is initialized by a random set of points as the center locations of the base Fresnel phase (green dots). The green edges mark the individual apertures. As the optimization evolves, the Voronoi-Fresnel cells tend to scatter uniformly in the design space, while a certain degree of irregularity of the apertures is maintained. When the optimization converges, an optimal phase profile is achieved. The best Voronoi-Fresnel phase profiles and MTFv values at iterations #1, #10, and #100 are shown in Fig. 2d. See Supplementary Movie 1 for an animation of the optimization process. After repeating the quasi-CVT step for different K values, the MTFv can be plotted against K , and a polynomial curve is fitted to the data. The maximum MTFv is found to occur when $K = 23$ in this example. Finally the optimal Voronoi-Fresnel phase is selected from the results in the best case of K .

A notable difference between our quasi-CVT algorithm and conventional CVT is that, a certain degree of irregularity should be preserved in quasi-CVT, while the CVT tends to converge to a regular hexagonal grid. Theoretically, the optimal CVT in a 2D plane results in a hexagonal pattern¹⁸. To demonstrate that the optimization is non-trivial, we compare the optimized result from the above algorithm against a regular rectangular and a hexagonal Voronoi-Fresnel phase. The design area is 256×256 pixels, and the number of cells is 64 in all three cases. The two regular grids are equivalent to common off-the-shelf microlens arrays. As shown in Fig. 3, the MTFv on the regular rectangular (MTFv = 1.14) or hexagonal grid (MTFv = 1.19) is significantly lower than the optimized result (MTFv = 2.29). This attributes to the fact that the regular grids lack of diversity in the directional filtering. Therefore, the optimization is non-trivial. Simple and regular off-the-shelf microlens arrays are not well-suited for this purpose.

The parameter sweep in the second step of the algorithm is time-consuming, especially when the design space is large. We can facilitate the search of best number of sites in the full scale from smaller scales. We evaluate the

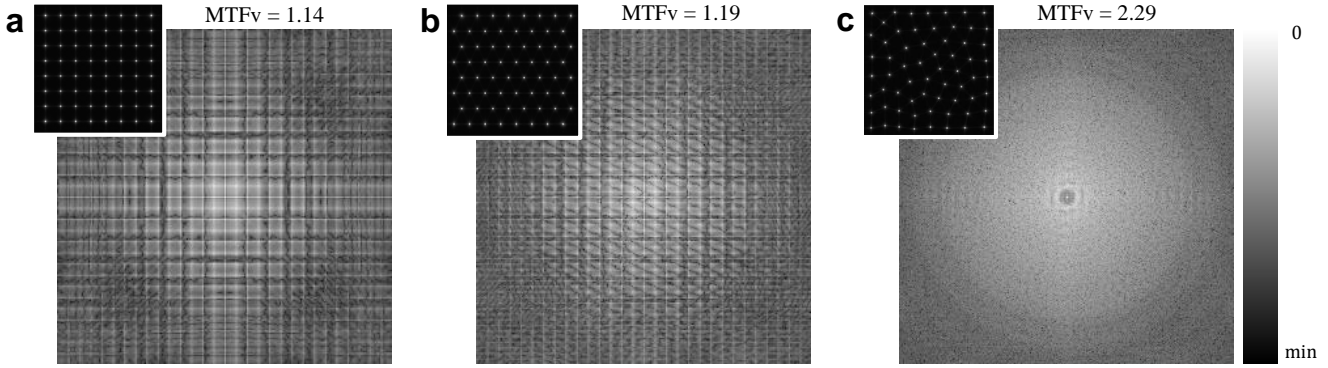


Fig. 3. MTF comparison of regular and optimized PSFs. Conventional solutions to the 2D CVT problem result in regular grids that are not necessarily optimal in MTFv. **a** and **b** show the log-scale panchromatic MTF for rectangular and hexagonal Voronoi-Fresnel phases respectively. Periodic patterns exist in both cases. **c** The optimized quasi-CVT shows more uniform frequency distribution and higher MTFv values. The corresponding PSFs are shown in the top-left corners in each case.

optimal K in various scales and plot the MTFv to the design area in Fig. 4. The result indicates the algorithm is linearly scalable with respect to the design area.

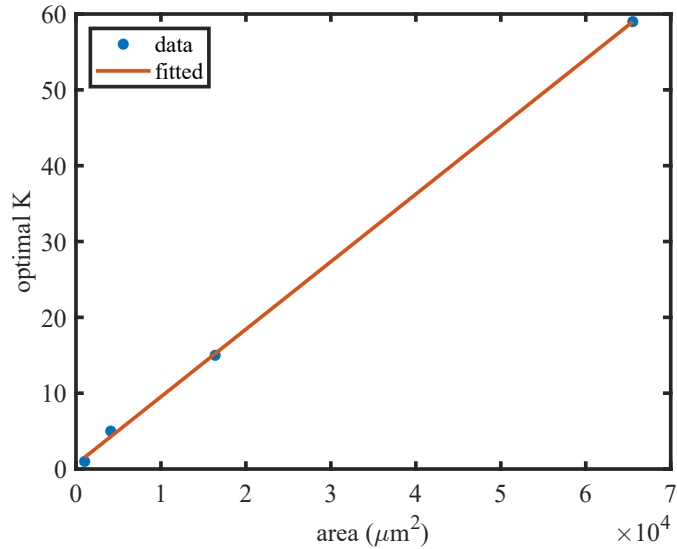


Fig. 4. Linear Scalability. The optimal number of Voronoi sites is linearly proportional to the design area.

Image reconstruction

We formulate the image formation process as a convolution between the ground-truth image and the PSF. We can rewrite the above image formation in the matrix-vector product form, $\mathbf{y} = \mathbf{Ax} + \mathbf{n}$, where $\mathbf{x} \in \mathbb{R}^{3N}$ is the ground-truth image with N pixels in three color channels, $\mathbf{A} \in \mathbb{R}^{3N \times 3N}$ is a Toeplitz matrix that represents the color PSFs, and $\mathbf{y} \in \mathbb{R}^{3N}$ is the captured raw data. The data is degraded by additive noise \mathbf{n} .

To take the spectral variations into account, we apply the convolution between spectral images and spectral PSFs before integrating them over the spectral range for each color channel. It is more accurate than using a color ground-truth image and a color PSF directly. The ground-truth color image is then defined by assuming the PSF is an ideal Dirac delta function in all color channels. See Methods for detailed descriptions.

The image reconstruction process is to solve an image deconvolution problem with a Total Variation (TV) regularization. The TV regularizer encourages the sparsity of edges in natural images, which has proven effective in

many image reconstruction tasks^{7, 20}, i.e.,

$$\arg \min_{\mathbf{x}} \frac{1}{2} \|\mathbf{Ax} - \mathbf{y}\|_2^2 + \mu \|\mathbf{Dx}\|_1, \quad (4)$$

where $\|\cdot\|_2$ and $\|\cdot\|_1$ are the ℓ_2 -norm and ℓ_1 -norm respectively. \mathbf{D} is the the finite difference operator, and μ is a penalization weight. TV regularized image deconvolution is convex but not differentiable. An effective way to solve this problem is to employ the Alternating Direction Method of Multipliers (ADMM)²¹. Detailed algorithm implementation, simulation results, and comparison with existing methods are provided in Supplementary Note 4.

Experimental results

A prototype Voronoi-Fresnel lensless camera is built with a board-level camera FLIR BFS-GE-16S2C-BD2 and a custom fabricated phase element using photolithography techniques (see Supplement 1). The image sensor (Sony IMX273) has 1440×1080 pixels, with a pixel pitch of $3.45 \mu\text{m}$. The optical distance in-between is 3 mm, where the cover glass on the sensor has a thickness of 0.7 mm. The sensor's angular response covers approximately $\pm 20^\circ \times \pm 15^\circ$ field-of-view, so the shift-invariance of the PSF should be maintained within this angular range. Marginal cells beyond the field-of-view are excluded for this purpose. The optimized phase profile is shown in Fig. 5a. The excluded cells are empty of the Fresnel phase. A calibration PSF is shown in Fig. 5b with a zoom-in area highlighting three adjacent spots. The optical element is fabricated on a 0.5-mm-thick fused silica substrate. At a nominal wavelength of 550 nm, the 2π phase modulation corresponds to a total depth of 1200 nm, which is discretized into 16-levels for fabrication. The lateral fabrication resolution is $1.15 \mu\text{m}$, making each sensor pixel upsampled by 3×3 optical pixels. The optical element is assembled onto the sensor by 3D-printed mechanical mounts, as shown in Fig. 5c. An optical microscope image (Nikon Eclipse L200N, 5 \times) and a 3D measurement (Zygo NewView 7300, 20 \times) of the fabricated sample are shown in Fig. 5d.

The captured raw data in the Voronoi-Fresnel lensless camera is a mixture of spatial object points in a well-structured way. Since each individual Voronoi-Fresnel cell makes a projected and shifted copy of different parts of the scene, the captured data are actually super-positioned sub-images. After reconstruction, the intensities from the mixed sub-images are re-arranged back to their original positions, and hence a conventional image is composited. In the following, we present the raw data in full sensor resolution, and the reconstructed images are cropped to 640×480 pixels to cover the $\pm 20^\circ \times \pm 15^\circ$ field-of-view. The object distance is about 30 cm away from the lensless camera.

We evaluate the image performance in two illumination scenarios. The first is self-illuminating images displayed on a computer monitor. Self-illuminating objects emit light in a confined angular range, so little stray light or cross-talk is introduced in the captured data. Fluorescence imaging would be a good application for this mode. Figure 5e and 5f show the captured raw data. The reconstructed image in Fig. 5i reveals fine details in the camera and human face. A zoom-in area of the camera object is shown in Fig. 5m. We evaluate the spatial resolution with a USAF resolution target in Fig. 5j, with two cross lines (yellow and magenta) plotted in Fig. 5n for the RGB color channels. Line pairs in the central area are clearly visible.

The second is real objects with ambient illumination, as shown in Fig. 5g and 5h. This is a more realistic scenario for photography outside of a lab environment or in applications like endoscopy. Ambient illumination poses a severe challenge for existing flat or lenseless imaging systems, since “stray” light can enter the camera at angles outside the nominal field of view, which is then not modeled by the reconstruction algorithm. We show the reconstructed car toy image example in Fig. 5k and a printed USAF resolution chart in Fig. 5l. Since the ambient illumination is not uniform across the scene, the intensity fall-off from on-axis to off-axis, which is vignetting, is more obvious than in the self-illuminating case. The recovered image is still able to reveal sufficient details despite of the complicated environmental light condition. Similarly we evaluate the spatial resolution with the printed USAF resolution target in Fig. 5j. The cross lines in Fig. 5p indicate that the line pairs can be discriminate very well in green and blue channels, while it becomes less reliable in the red channel in the high frequency line pairs. The differences in color channels also indicate residual chromatic aberrations exist in the reconstructed images. More characteristic tests and real object imaging results for the prototype are presented in Supplementary Note 5.

Discussion

Existing lensless cameras either focuses on bioinspired compound-eye optical layout (e.g., metasurface ommatidia²²) or heuristic PSF engineering e.g., DiffuserCam⁷ and PhlatCam⁸. The proposed Voronoi-Fresnel lensless camera differentiates itself from both compound-eye and PSF engineering. First, although the base first-order Fresnel phase is a mimicry of the ommatidium in apposition compound eyes, its distribution across the planar area is neither

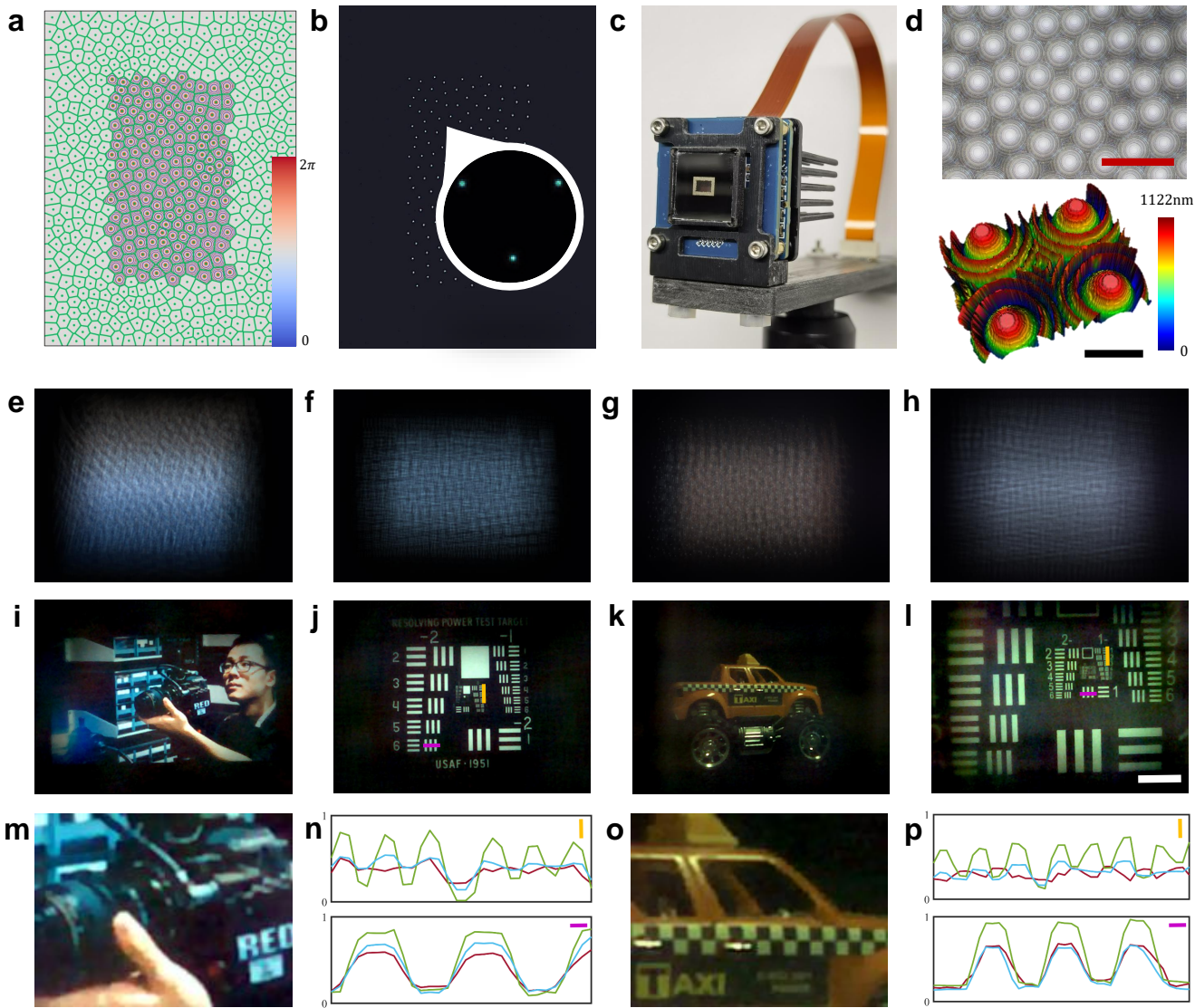


Fig. 5. Experimental results with the prototype Voronoi-Fresnel lensless camera. **a** Optimized phase profile with a field-of-view of $\pm 20^\circ$. Cell boundaries are marked by the overlaid green polygons. Marginal Voronoi-Fresnel cells are excluded to maintain the shift-invariance of the PSF. **b** Calibrated color PSF (brightness enhanced) with the magnified area showing three adjacent spots. **c** The prototype consists of a Voronoi-Fresnel phase element mounted with 3D-printed parts onto a board-level sensor. **d** Top is a $5\times$ microscopic image of the fabricated 16-level sample on a Nikon Eclipse L200N microscope. Scale bar is $300\ \mu\text{m}$. Bottom is a $20\times$ microstructure measurement on a Zygo NewView 7300 profilometer. Scale bar is $100\ \mu\text{m}$. **e** and **f** are the raw data for the scenes displayed on a computer monitor, and **i**, **j** are the reconstructed images respectively. **m** is the zoom-in area in **i**, and **n** represents the intensity profile along the colored lines in USAF resolution chart in reconstruction **j**. **g** and **h** represent the raw data the real objects taken under ambient illumination. The reconstructed images are **k** and **l** respectively. **o** is the zoom-in area in **k**, and **p** shows the corresponding cross line in the real resolution chart in **l**.

random nor regular, but optimized to yield optimal performance. Second, the overall PSF is not engineered directly from a single phase profile, but a composition of various directional filters from individual sub-aperture's diffraction patterns. This facilitates large-area design in high spatial resolution, which alleviates the sampling load for the phase element on mega-pixel sensors. The smooth microstructures ease fabrication requirements than otherwise high-frequency random features in heuristic designs. Finally, the Voronoi-Fresnel lensless camera finds an in-between strategy that takes advantages of both compound-eye and PSF engineering methods. The resulting Voronoi-Fresnel

phase is capable of superior image quality with cost-effective hardware design.

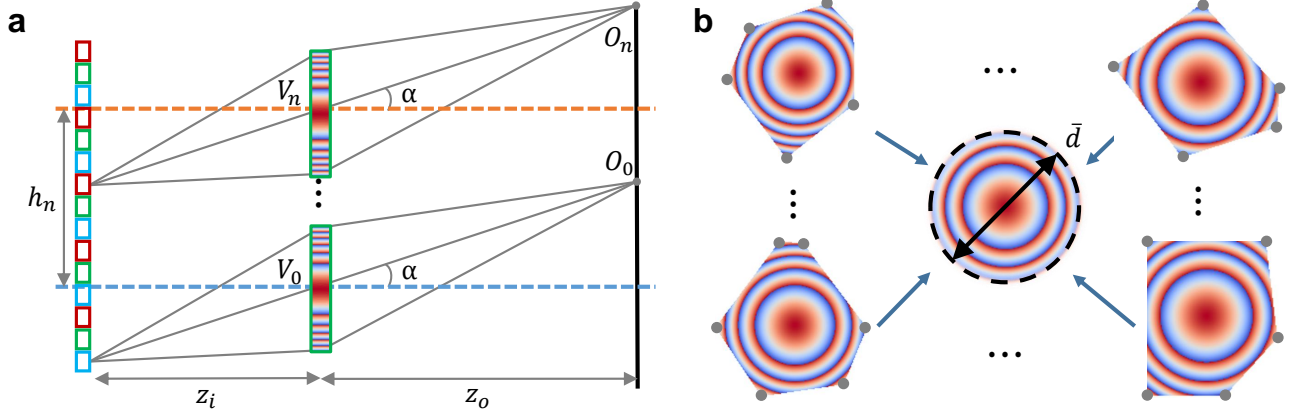


Fig. 6. Field-of-view and limiting resolution analysis. **a** The field-of-view is determined by the sensor cut-off angle, marginal Voronoi-Fresnel cell displacement, and the object distance. **b** The statistical diameter of the base Fresnel phase is the root-sum-square distance from the vertices to their respective center locations.

Compared to its lens counterparts, the performance of the Voronoi-Fresnel lensless imaging can also be characterized and analyzed by effective focal length, spatial resolution, field-of-view and so on. Since the Voronoi-Fresnel phase is a collection of the same base Fresnel phase, the effective focal length is also the focal length of the base Fresnel phase. The field-of-view is determined by three factors, as shown in Fig. 6a. First, the image sensor usually has a cut-off angle α , beyond which light is not sensible. Each Voronoi-Fresnel cell is limited by this cut-off angle. The outmost object that the central cell V_0 can see is O_0 in the object space. Second, the marginal cell has a lateral center displacement h_n from the optical axis. This corresponds to an angular displacement of $\arctan(h_n/z_o)$. The equivalent half field-of-view is then

$$\theta = \alpha + \arctan\left(\frac{h_n}{z_o}\right) = \alpha + \arctan\left(\frac{mh_n}{z_i}\right), \quad (5)$$

where $m = z_i/z_o$ is the magnification.

The resolution of lensless cameras is usually object-dependent. Since the base Fresnel phase is a first-order approximation of an ideal lens, the individual cell is closely diffraction-limited. There exists a theoretical limiting resolution. However, variations in the aperture shapes do exist between different Voronoi-Fresnel cells. We define an effective diameter \bar{d} for the base Fresnel phase by statistically calculating the Root-Sum-Square (RSS) distance of all the vertices to their respective center locations. Assuming the i -th cell has M_i vertices, and there are N cells in total, the RSS diameter is

$$\bar{d} = 2\sqrt{\frac{\sum_{i=1}^N \sum_{j=1}^{M_i} (x_i^j - x_i)^2 + (y_i^j - y_i)^2}{\sum_{i=1}^N M_i}}, \quad (6)$$

where (x_i, y_i) are the i -th center coordinates, and (x_i^j, y_i^j) are the j -th vertex in the i -th cell. The equivalent limiting resolution can be evaluated according to the conventional Rayleigh criterion, i.e., $1.22\lambda z_i/\bar{d}$. In practice, the final image quality is degraded by the complexity of the scene, the noise, and the algorithm efficacy. In addition, MTF offers another perspective to analyze the resolution. Owing to the blue-noise sampling, the optimized MTF shows minimal low-frequency components, while keeping mid-frequency and high-frequency well. This indicates the contrast in smooth objects is sacrificed to allow more mid-frequency and high-frequency information to be recorded.

The proposed Voronoi-Fresnel lensless camera also exhibits a few limitations. First, the two-step optimization algorithm is time-consuming due to the parameter sweep step. Although the scalability property helps estimating the correct range, it is still expected to develop more efficient algorithms to accelerate the process for large-area designs. Second, the FOV is currently limited by the cut-off angle of the sensor, which is mainly due to the microlens array embedded in the image sensor. The intensity fall-off may be a concern for wide-angle applications. It may

be possible to design telecentric Voronoi-Fresnel to mitigate the situation, although fabrication complexity would be increased. Another limitation for the current prototype is the stray light. A common practice in conventional lenses to control stray light is to use baffles. However, it is difficult to implement such an idea without sacrificing the compactness. In the apposition type compound eyes, evolution has developed a screening pigment around the ommatidium to block stray light and cross-talk from entering the photoabsorbing rhabdom. Similar structures can be fabricated by etching deep trenches around the boundaries of Voronoi-Fresnel cells, and fill in black materials.

We have demonstrated a compound eye inspired lensless camera with optimal information preservation in optics. Following the proposed Fourier domain metric MTFv, we are able to tailor a spatially-coded Voronoi-Fresnel phase for better computational image reconstruction. Experimental results show the superior image quality of the prototype lensless camera in various illumination conditions. The advantages of the proposed Voronoi-Fresnel lensless camera offer a simple yet cost-effective imaging solution to significantly reducing the volume of imaging devices. The possibility of mass production makes it a promising candidate in applications such as fluorescence imaging, endoscopy, and internet-of-things.

Methods

Voronoi-Fresnel phase optimization.

For incoherent monochromatic light, the spectral PSF is the squared magnitude of the Voronoi-Fresnel phase's Fresnel diffraction pattern,

$$\mathbf{PSF}(x, y, \lambda) = |\mathcal{F}_z \{\Phi(\xi, \eta, \lambda)\}|^2, \quad (7)$$

where $\mathcal{F}_z \{\cdot\}$ is the Fresnel propagator for a distance z . Specifically, the diffraction pattern on the sensor plane reads

$$P(x, y, \lambda) = \frac{1}{j\lambda z} \iint \Phi(\xi, \eta, \lambda) \exp\left(j\frac{\pi}{\lambda z} \left((x - \xi)^2 + (y - \eta)^2\right)\right) d\xi d\eta. \quad (8)$$

We can obtain the the complex light field by substituting Eq. (1) into the above Fresnel propagator. Since the Voronoi-Fresnel phase is a collection of independent Fresnel phase, and Fresnel diffraction is a linear operator, the resulting diffraction pattern is also a collection of individual Fresnel diffraction patterns offset by their center locations. In addition, the propagation distance is equal to the distance in the quadratic terms of the base Fresnel phase, so the diffraction patterns essentially become the Fourier transform of the shifted aperture functions. As derived in Supplementary Note 1, each diffraction pattern is

$$P_i(x, y, \lambda) = \frac{C(\xi_i, \eta_i)}{j\lambda z} \mathcal{F}\{A_i(\xi, \eta)\} \Big|_{\left[\frac{x-\xi_i}{\lambda z}, \frac{y-\eta_i}{\lambda z}\right]}, \quad (9)$$

where $C(\xi_i, \eta_i)$ is a constant quadratic phase term, and the Fourier transform is evaluated at frequencies of $[(x - \xi_i)/\lambda z, (y - \eta_i)]$. The overall effective PSF is

$$\mathbf{PSF}(x, y, \lambda) = \left| \sum_{i=1}^K P_i(x, y, \lambda) \right|^2. \quad (10)$$

Since $V_i \cap V_j = \emptyset, \forall i \neq j$, all the apertures are independent and have no overlapped areas with each other. The cross terms in Eq. (10) diminish (see Supplementary Note 1), so

$$\mathbf{PSF}(x, y, \lambda) = \sum_{i=1}^K |P_i(x, y, \lambda)|^2 = \sum_{i=1}^K \mathbf{PSF}_i(x, y, \lambda) = \sum_{i=1}^K \mathbf{PSF}_i^0(x - \xi_i, y - \eta_i, \lambda), \quad (11)$$

where $\mathbf{PSF}_i^0(x, y, \lambda)$ is the centered PSF as if the aperture were at the origin of the design space. The panchromatic PSF is the integral of the spectral PSFs over the spectral range, as indicated in Eq. (2).

MTF is the magnitude of the Fourier transform of the PSF. As derived in the Supplementary Note 2, it can be written as

$$\mathbf{MTF}(f_X, f_Y, \lambda) = \left| \sum_{i=1}^K \mathbf{OTF}_i^0(f_X, f_Y, \lambda) \exp(-j f_X \xi_i, -j f_Y \eta_i) \right|, \quad (12)$$

where f_X and f_Y are the Fourier domain frequencies. The individual OTFs in the complex form are $\mathbf{OTF}_i^0(\lambda) = \mathcal{M}_i(\lambda) \exp(\mathcal{P}_i(\lambda))$, where the frequencies are omitted for brevity. The remaining phase delay terms are simplified as $\exp(-j\Psi_i) = \exp(-j f_X \xi_i, -j f_Y \eta_i)$, so the MTF can be rewritten as

$$\mathbf{MTF}(f_X, f_Y, \lambda) = \left| \sum_{i=1}^K \mathcal{M}_i(\lambda) \exp(-j\mathcal{P}_i(\lambda)) \exp(-j\Psi_i) \right|. \quad (13)$$

The panchromatic MTFv is an integral of the MTFs over all the frequencies and wavelengths, as shown in Eq. (3).

Our solution to the Voronoi-Fresnel phase optimization is based on the above conjecture that the optimal center locations would require uniform distributions of the Voronoi cells over the 2D design space, as well as keeping some degrees of irregularity of each Voronoi region to diversify the spatial filtering of individual PSFs. We adopt the CVT method for blue-noise sampling of the center locations, and propose a two-step optimization algorithm to maximize the panchromatic MTFv. A background of the CVT method is explained in Supplementary Note 3. The first step is a quasi-CVT optimization, as summarized in Algorithm 1. To make the algorithm fabrication-aware, we set the terminating tolerance tol as a hundredth of the smallest feature size that can be fabricated. Smaller tolerances contribute little to the convergence, but add much to the manufacture difficulties. The iterations terminate after a maximum number of iterations $maxiter$ is reached. The second step is simply a parameter sweep to find the best K .

Algorithm 1: Maximize MTFv for a given K

```

input : number of Voronoi regions  $K$ 
         fabrication parameters
          $maxiter, tol$ 
output : Voronoi sites coords
          $maxMTFv$ 

1 generate  $K$  random points  $\{\mathbf{p}_i\}_{i=1}^K$ ;
2 construct Voronoi tessellation  $\{V_i\}_{i=1}^K$ ;
3 compute MTFv by Eq. (3);
4 coords  $\leftarrow \{\mathbf{p}_i\}_{i=1}^K$ ;
5  $maxMTFv \leftarrow MTFv$ ;
6 for  $k \leq maxiter$  do
7   | compute mass centroids  $\mathbf{c}_i$  for  $\{V_i\}_{i=1}^K$ ;
8   | update  $\{\mathbf{p}_i\}_{i=1}^K \leftarrow \{\mathbf{c}_i\}_{i=1}^K$ ;
9   | construct new Voronoi tessellation;
10  | compute new  $MTFv$ ;
11  | if  $MTFv > maxMTFv$  then
12    |   | coords  $\leftarrow \{\mathbf{p}_i\}_{i=1}^K$ ;
13    |   |  $maxMTFv \leftarrow MTFv$ ;
14  | else
15    |   | continue;
16  | end
17  |  $error = \sqrt{\frac{1}{K} \sum_{i=1}^K \|\mathbf{p}_i^k - \mathbf{p}_i^{k-1}\|^2}$ ;
18  | if  $error < tol$  then
19    |   | break;
20  | end
21 end

```

Image formation and reconstruction.

A color image recorded on the image sensor is an integral of spectrally-blurred images weighted by the color response of the sensor. This process can be expressed as

$$g_c(x, y) = \int_{\lambda_1}^{\lambda_2} q_c(\lambda) (f(x, y, \lambda) * h(x, y, \lambda)) d\lambda, \quad (14)$$

where $f(x, y, \lambda)$ is the latent spectral image at wavelength λ , $h(x, y, \lambda)$ is the spectral PSF in Eq. (11), and $*$ denotes spatial convolution. $q_c(\lambda)$ is the color response function of the sensor, and $g_c(x, y)$ is the captured color image in color channel c (for sensors with Bayer filters, $c = r, g, b$).

If the imaging system is perfect, we assume the spectral PSFs are all identically Dirac delta functions, i.e., $h(x, y, \lambda) = \delta(x, y, \lambda) = \delta(x, y)$. The ground-truth sharp image would be

$$f_c(x, y) = \int_{\lambda_1}^{\lambda_2} q_c(\lambda) f(x, y, \lambda) d\lambda. \quad (15)$$

On the other hand, if the image is a spectrally-uniform ideal point source, $f(x, y, \lambda) = \delta(x, y, \lambda) = \delta(x, y)$, the captured image would be a color PSF

$$h_c(x, y) = \int_{\lambda_1}^{\lambda_2} q_c(\lambda) h(x, y, \lambda) d\lambda. \quad (16)$$

Note that if the imaging system is approximately achromatic, $h(x, y, \lambda) \approx h(x, y)$, Eq. (14) can be simplified by

$$\begin{aligned} g_c(x, y) &\approx \left(\int_{\lambda_1}^{\lambda_2} q_c(\lambda) f(x, y, \lambda) d\lambda \right) * h(x, y) \\ &= f_c(x, y) * \int_{\lambda_1}^{\lambda_2} q_c(\lambda) h(x, y) d\lambda \\ &= f_c(x, y) * h_c(x, y), \end{aligned} \quad (17)$$

where the sensor response is normalized such that $\int_{\lambda_1}^{\lambda_2} q_c(\lambda) d\lambda = 1$. To solve a minimization problem in the ADMM framework, we introduce a slack variable $\mathbf{z} = \mathbf{Dx}$, and apply the augmented Lagrangian multiplier,

$$\arg \min_{\mathbf{x}} \frac{1}{2} \|\mathbf{Ax} - \mathbf{y}\|_2^2 + \mu \|\mathbf{z}\|_1 + \frac{\rho}{2} \|\mathbf{Dx} - \mathbf{z}\|_2^2, \quad (18)$$

where ρ is the weight for the slack variable. The ADMM iterations consist of three steps,

$$\begin{cases} \mathbf{x}^{k+1} = \arg \min_{\mathbf{x}} \frac{1}{2} \|\mathbf{Ax} - \mathbf{y}\|_2^2 + \frac{\rho}{2} \|\mathbf{Dx} - \mathbf{z} + \mathbf{u}\|_2^2 \\ \mathbf{z}^{k+1} = \arg \min_{\mathbf{z}} \mu \|\mathbf{Dx} - \mathbf{z}\|_1 + \frac{\rho}{2} \|\mathbf{Dx} - \mathbf{z} + \mathbf{u}\|_2^2 \\ \mathbf{u}^{k+1} = \mathbf{u}^k + \mathbf{Dx}^{k+1} - \mathbf{z}^{k+1}, \end{cases} \quad (19)$$

where \mathbf{u} is the scaled dual variable. The \mathbf{x} -problem can be efficiently solved in the Fourier domain. The analytical solution is

$$\mathbf{x}^{k+1} = (\mathbf{A}^T \mathbf{A} + \rho \mathbf{D}^T \mathbf{D})^{-1} (\mathbf{A}^T \mathbf{A} + \rho \mathbf{D}^T \mathbf{D}) \mathbf{y}. \quad (20)$$

The \mathbf{z} -problem has a closed-form solution,

$$\mathbf{z}^{k+1} = \mathcal{S}_{\mu/\rho}(\mathbf{Dx}^{k+1} + \mathbf{u}^k), \quad (21)$$

where $\mathcal{S}_\kappa(v) = (1 - \kappa/|v|)_+ v$ is an element-wise soft thresholding operator. Finally \mathbf{u} is updated with the new \mathbf{x} and \mathbf{z} . The detailed implementation of the image reconstruction pipeline is discussed in Supplementary Note 4.

Fabrication.

The experimental samples are fabricated by a combination of photolithography and reactive-ion etching (RIE) techniques. The substrate is a 4 inch fused silica wafer with a thickness of 0.5 mm. We binarize the optimized Voronoi-Fresnel phase profile into $2^4 = 16$ levels, and repeat 4 iterations of the basic photolithography with different masks and then RIE with doubled etching time. The masks are fabricated on soda lime substrates by laser direct writing on a Heidelberg μ PG 501 mask maker. In each iteration, the wafer is first cleaned in Piranha solution at 115°C for 10 min, and dried with N₂. A 150-nm-thick Chromium (Cr) layer is deposited by sputtering on one side of the wafer. A 0.6- μ m-thick layer of photoresist AZ1505 is then spin-coated on top of Cr after HMDS

(Hexamethyldisilazane) vapor priming. To transfer the mask patterns to the wafer, we align the wafer with the mask on a contact aligner EVG6200 ∞ in the hard+vacuum mode, and then apply UV exposure with a dose of 9 mJ/cm². The photoresist is developed in AZ726MIF developer (2.38% TMAH in H₂O) for 20 sec before De-Ionized water clean and N₂ drying. To transfer the patterns from the photoresist to the Cr layer, we wet etching the wafer with Cr etchant (mixtures of HClO₄ and (NH₄)₂[Ce(NO₃)₆]) for 1 min and remove the residual photoresist with Acetone. In the RIE step, SiO₂ in the wafer is etched by plasma of 15 sccm CHF₃ and 5 sccm O₂ at 10 °C. The etching depths are 75 nm, 150 nm, 300 nm and 600 nm respectively for a design wavelength at 550 nm. An additional Cr layer is deposited and etched to serve as the aperture to preserve the shift-invariance of PSFs.

PSF Calibration.

The PSF is calibrated by placing a pinhole in front of the lensless camera. We use a lever-actuated iris diaphragm (Thorlabs SM1D12) with the diameter adjusted at 0.8 mm as a pinhole. The distances between the pinhole and the prototype for calibration are 30 cm and 50 cm respectively. A plasma white light source with a liquid light guide (Thorlabs HPLS245) is used for the pinhole illumination.

References

1. Schoenemann, B., Pärnaste, H. & Clarkson, E. N. Structure and function of a compound eye, more than half a billion years old. *Proc. Natl. Acad. Sci. U.S.A.* **114**, 13489–13494 (2017).
2. Cheng, Y., Cao, J., Zhang, Y. & Hao, Q. Review of state-of-the-art artificial compound eye imaging systems. *Bioinspir. Biomim.* **14**, 031002 (2019).
3. Lee, G. J., Choi, C., Kim, D.-H. & Song, Y. M. Bioinspired artificial eyes: optic components, digital cameras, and visual prostheses. *Adv. Funct. Mater.* **28**, 1705202 (2018).
4. Song, Y. M. *et al.* Digital cameras with designs inspired by the arthropod eye. *Nature* **497**, 95–99 (2013).
5. Floreano, D. *et al.* Miniature curved artificial compound eyes. *Proc. Natl. Acad. Sci. U.S.A.* **110**, 9267–9272 (2013).
6. Asif, M. S., Ayrem lou, A., Sankaranarayanan, A., Veeraraghavan, A. & Baraniuk, R. G. Flatcam: Thin, lensless cameras using coded aperture and computation. *IEEE Trans. Comput. Imaging* **3**, 384–397 (2016).
7. Antipa, N. *et al.* DiffuserCam: lensless single-exposure 3D imaging. *Optica* **5**, 1–9 (2018).
8. Boominathan, V., Adams, J., Robinson, J. & Veeraraghavan, A. Phlatcam: Designed phase-mask based thin lensless camera. *IEEE Trans. Pattern Anal. Mach. Intell.* (2020).
9. Wu, J. *et al.* Single-shot lensless imaging with fresnel zone aperture and incoherent illumination. *Light. Sci. Appl.* **9**, 1–11 (2020).
10. Cai, Z. *et al.* Lensless light-field imaging through diffuser encoding. *Light. Sci. Appl.* **9**, 1–9 (2020).
11. Goodman, J. W. *Introduction to Fourier optics* (Roberts and Company Publishers, 2005).
12. Yan, D.-M., Guo, J.-W., Wang, B., Zhang, X.-P. & Wonka, P. A survey of blue-noise sampling and its applications. *J Comput. Sci. Technol.* **30**, 439–452 (2015).
13. De Goes, F., Breeden, K., Ostromoukhov, V. & Desbrun, M. Blue noise through optimal transport. *ACM Trans. Graph.* **31**, 1–11 (2012).
14. Du, Q., Faber, V. & Gunzburger, M. Centroidal Voronoi tessellations: Applications and algorithms. *SIAM Rev. Soc. Ind. Appl. Math.* **41**, 637–676 (1999).
15. Lanaro, M. P., Perrier, H., Coeurjolly, D., Ostromoukhov, V. & Rizzi, A. Blue-noise sampling for human retinal cone spatial distribution modeling. *J. Phys. Commun.* **4**, 035013 (2020).
16. Kim, S., Cassidy, J. J., Yang, B., Carthew, R. W. & Hilgenfeldt, S. Hexagonal patterning of the insect compound eye: Facet area variation, defects, and disorder. *Biophys. J.* **111**, 2735–2746 (2016).
17. Vanhoutte, K. J., Michielsen, K. F. & Stavenga, D. G. Analyzing the reflections from single ommatidia in the butterfly compound eye with Voronoi diagrams. *J. Neurosci. Methods* **131**, 195–203 (2003).
18. Yan, D.-M., Wang, K., Lévy, B. & Alonso, L. Computing 2D periodic centroidal voronoi tessellation. In *2011 Eighth International Symposium on Voronoi Diagrams in Science and Engineering*, 177–184 (IEEE, 2011).
19. Lloyd, S. Least squares quantization in PCM. *IEEE Trans. Inf. Theory* **28**, 129–137 (1982).

20. Boominathan, V. *et al.* Lensless imaging: A computational renaissance. *IEEE Signal Process. Mag.* **33**, 23–35 (2016).
21. Boyd, S., Parikh, N. & Chu, E. *Distributed optimization and statistical learning via the alternating direction method of multipliers* (Now Publishers Inc, 2011).
22. Kogos, L. C. *et al.* Plasmonic ommatidia for lensless compound-eye vision. *Nat. Commun.* **11**, 1–9 (2020).

Acknowledgements

This work was supported by King Abdullah University of Science and Technology (Individual Baseline Funding). D.Y. was also supported by National Natural Science Foundation of China (62172415) and National Key Research and Development Program of China (2019YFB2204104).

Author contributions statement

Q.F. conceived the idea. Q.F. and D.Y. developed the algorithms. Q.F. constructed the prototype and conducted the experiments. D.Y. and W.H. analyzed the results. W.H. coordinated and instructed the project. All authors wrote and reviewed the manuscript.

Competing interests

The authors declare no competing interests.

Data availability

The data that support the findings of this study are available from the corresponding authors upon reasonable request.

Code availability

The source code is available from the corresponding authors upon reasonable request.

Additional information

Supplementary information is available for this paper.

Correspondence and requests for materials should be addressed to Q.F. or W.H.

Compound eye inspired flat lensless imaging with spatially-coded Voronoi-Fresnel phase: Supplementary Information

Qiang Fu^{1,*}, Dong-Ming Yan^{2,3}, and Wolfgang Heidrich^{1,*}

¹King Abdullah University of Science and Technology, Thuwal, 23955-6900, Saudi Arabia

²National Laboratory of Pattern Recognition (NLPR), Institute of Automation, Chinese Academy of Sciences, 100190, Beijing, China

³School of AI, University of Chinese Academy of Sciences, China

*Corresponding authors: qiang.fu@kaust.edu.sa, wolfgang.heidrich@kaust.edu.sa.

Supplementary Note 1. Point Spread Function

In this note, we derive the mathematical expression of the point spread functions (PSFs) as shown in Eq. (2) in the main texts. For each Voronoi-Fresnel cell, the complex optical field after propagating from the phase element to the image sensor plane is

$$\begin{aligned}
 P_i(x, y, \lambda) &= \mathcal{F}_z \left\{ A_i(\xi - \xi_i, \eta - \eta_i) \exp \left(-j \frac{2\pi}{\lambda} \frac{(\xi - \xi_i)^2 + (\eta - \eta_i)^2}{2z} \right) \right\} \\
 &= \frac{1}{j\lambda z} \iint A_i(\xi', \eta') \exp \left(-j \frac{\pi}{\lambda z} (\xi'^2 + \eta'^2) \right) \exp \left(j \frac{\pi}{\lambda z} ((x - \xi_i - \xi')^2 + (y - \eta_i - \eta')^2) \right) d\xi' d\eta' \\
 &= \frac{\exp \left(\frac{\pi}{\lambda z} ((x - \xi_i)^2 + (y - \eta_i)^2) \right)}{j\lambda z} \iint A_i(\xi', \eta') \exp \left(-j \frac{2\pi}{\lambda z} ((x - \xi_i) \xi' + (y - \eta_i) \eta') \right) d\xi' d\eta' \quad (S1) \\
 &= \frac{\exp \left(\frac{\pi}{\lambda z} ((x - \xi_i)^2 + (y - \eta_i)^2) \right)}{j\lambda z} \mathcal{F} \{ A_i(\xi', \eta') \} \Big|_{\left[\frac{x - \xi_i}{\lambda z}, \frac{y - \eta_i}{\lambda z} \right]} \\
 &= \frac{C(\xi_i, \eta_i)}{j\lambda z} \mathcal{F} \{ A_i(\xi', \eta') \} \Big|_{\left[\frac{x - \xi_i}{\lambda z}, \frac{y - \eta_i}{\lambda z} \right]},
 \end{aligned}$$

where we have replaced the variables by $\xi' = \xi - \xi_i$ and $\eta' = \eta - \eta_i$ in the second line. The integral in the third line is exactly the Fourier transform of the aperture function A_i evaluated at spatial frequencies $[(x - \xi_i)/\lambda z, (y - \eta_i)/\lambda z]$. The corresponding PSF is then

$$\begin{aligned}
 \mathbf{PSF}_i(x, y, \lambda) (x, y, \lambda) &= |P_i(x, y, \lambda)|^2 \\
 &\propto \left| \mathcal{F} \{ A_i(\xi', \eta') \} \Big|_{\left[\frac{x - \xi_i}{\lambda z}, \frac{y - \eta_i}{\lambda z} \right]} \right|^2 \\
 &= \mathbf{PSF}_i^0(x - \xi_i, y - \eta_i, \lambda),
 \end{aligned} \quad (S2)$$

where we denote $\mathbf{PSF}_i^0(x, y, \lambda)$ as the centered PSF as if the aperture were located at the origin,

$$\begin{aligned}
 \mathbf{PSF}_i^0(x, y, \lambda) &\propto |\mathcal{F} \{ A_i(\xi', \eta') \}|^2 \\
 &= \left| \iint A_i(\xi', \eta') \exp \left(-j \frac{2\pi}{\lambda z} (x\xi' + y\eta') \right) d\xi' d\eta' \right|^2.
 \end{aligned} \quad (S3)$$

This implies that the PSF for the i -th Voronoi-Fresnel cell is a shifted version of the centered PSF. It is worth noting that the shape and distribution of the centered PSF depend on the geometry of the aperture functions. These apertures are finite-edge polygons, so the centered PSFs are actually compact yet highly directional filters. It is important to diversify such directional filtering of the PSFs to achieve optimal performance.

The effective PSF of the Voronoi-Fresnel lensless camera is obtained in the same way by taking all the individual diffraction patterns into account,

$$\begin{aligned}
\mathbf{PSF}(x, y, \lambda) &= \left| \sum_{i=1}^K P_i(x, y, \lambda) \right|^2 \\
&= \left(\sum_{i=1}^K P_i^*(x, y, \lambda) \right) \left(\sum_{i=1}^K P_i(x, y, \lambda) \right) \\
&= \sum_{i=1}^K |P_i(x, y, \lambda)|^2 + \sum_{j=1}^K \sum_{i=1}^K P_i^*(x, y, \lambda) P_j(x, y, \lambda).
\end{aligned} \tag{S4}$$

Since the Voronoi cells share no intersections, $V_i \cap V_j = \emptyset, \forall i \neq j$, the individual aperture functions have no overlapped areas. The diffraction patterns $P_i(x, y, \lambda)$ and $P_j(x, y, \lambda)$ have no overlapped integrating areas, according to Eq. (S1), so the cross terms in Eq.(S4) are all zeros. Hence,

$$\begin{aligned}
\mathbf{PSF}(x, y, \lambda) &= \sum_{i=1}^K |P_i(x, y, \lambda)|^2 \\
&= \sum_{i=1}^K \mathbf{PSF}_i(x, y, \lambda) \\
&= \sum_{i=1}^K \mathbf{PSF}_i^0(x - \xi_i, y - \eta_i, \lambda),
\end{aligned} \tag{S5}$$

The above PSF is for monochromatic light. To get the panchromatic PSF, we simply integrate all the spectral PSFs over the interested spectral range,

$$\mathbf{PSF}(x, y) = \int_{\lambda_1}^{\lambda_2} \mathbf{PSF}(x, y, \lambda) d\lambda. \tag{S6}$$

Supplementary Note 2. Modulation Transfer Function

In this note, we provide a detailed derivation and analysis for the Modulation Transfer Function (MTF). Since an optical system is essentially a low-pass filter in the frequency domain, it is better to evaluate the PSF through its frequency counterpart, Modulation Transfer Function (MTF). MTF is the magnitude of the Optical Transfer Function (OTF), which is the Fourier transform of the PSF for incoherent imaging systems,

$$\mathbf{MTF} = |\mathbf{OTF}| = |\mathcal{F}\{\mathbf{PSF}\}|, \tag{S7}$$

where $0 \leq \mathbf{MTF} \leq 1$.

We can obtain the MTF by taking the Fourier transform of the PSF,

$$\begin{aligned}
\mathbf{MTF}(f_X, f_Y, \lambda) &= |\mathcal{F}\{\mathbf{PSF}(x, y, \lambda)\}| \\
&= \left| \sum_{i=1}^K \mathcal{F}\{\mathbf{PSF}_i^0(x - \xi_i, y - \eta_i, \lambda)\} \right| \\
&= \left| \sum_{i=1}^K \mathcal{F}\{\mathbf{PSF}_i^0(x, y, \lambda)\} \exp(-j f_X \xi_i, -j f_Y \eta_i) \right| \\
&= \left| \sum_{i=1}^K \mathbf{OTF}_i^0(f_X, f_Y, \lambda) \exp(-j f_X \xi_i, -j f_Y \eta_i) \right|,
\end{aligned} \tag{S8}$$

where f_X and f_Y are the Fourier domain frequencies, and we have applied the translation property of Fourier transform. The individual OTFs in the complex form are

$$\mathbf{OTF}_i^0(\lambda) = \mathcal{M}_i(\lambda) \exp(\mathcal{P}_i(\lambda)), \tag{S9}$$

where the frequencies are omitted for brevity. The remaining phase delay terms are simplified as $\exp(-j\Psi_i) = \exp(-jfx\xi_i, -jfy\eta_i)$, so the MTF can now be rewritten as

$$\text{MTF}(f_X, f_Y, \lambda) = \left| \sum_{i=1}^K \mathcal{M}_i(\lambda) \exp(-j\mathcal{P}_i(\lambda)) \exp(-j\Psi_i) \right|. \quad (\text{S10})$$

This equation reveals the three factors that affect the MTF, the diffraction by each similar apertures that determined the $|\mathcal{M}(\lambda)|$ term; the phase difference terms $(\Psi_i - \Psi_j)$ introduced by the amount of shifts from the centered PSFs; and the total number of Voronoi-Fresnel cells K .

Supplementary Note 3. Centroidal Voronoi Tessellation

Finding the optimal tessellation of the 2D design space is basically a sampling problem. Among various sampling methods, blue noise sampling^{1,2} offers minimal low-frequency components and no concentrated spikes of energy, which is the required properties for our lensless DOE application. An effective way to achieve blue noise sampling is by Centroidal Voronoi Tessellation (CVT)³. The CVT is a special Voronoi diagram where the sites coincide with the mass centroids of the corresponding Voronoi regions. The mass centroid of a Voronoi region V_i is defined as

$$\mathbf{c}_i = \frac{\int_{V_i} \mathbf{p} \tau(\mathbf{p}) d\mathbf{p}}{\int_{V_i} \tau(\mathbf{p}) d\mathbf{p}}, \quad (\text{S11})$$

where \mathbf{p} is a point in the Cartesian coordinates, and τ is a given density function. We can assume a constant density across the 2D plane for simplicity, i.e., $\tau \equiv 1$. CVT is a critical point of the energy function defined by

$$E_{\text{CVT}}(P) = \sum_{i=1}^K \int_{V_i} \tau(\mathbf{p}) \|\mathbf{p} - \mathbf{p}_i\|^2 d\mathbf{p}. \quad (\text{S12})$$

There are various algorithms to optimize the above energy function and generate optimal CVT^{3,4}. A classic method is to use Lloyd iterations⁵ to update the Voronoi sites by their centroids until convergence. In each iteration, the mass centroids are computed for the current Voronoi regions. Then these generating sites are replaced by the calculated centroids, and a new Voronoi tessellation is constructed. The process is repeated until a convergence criterion is met. The Lloyd's algorithm is summarized in Supplementary Algorithm S1.

Algorithm S 1: Lloyd's iteration for CVT

```

input : number of Voronoi regions  $K$ 
        density function  $\tau$ 
output : Voronoi sites

1 generate  $K$  random points  $\{\mathbf{p}_i\}_{i=1}^K$ ;
2 construct Voronoi tessellation  $\{V_i\}_{i=1}^K$ ;
3  $\text{coords} \leftarrow \{\mathbf{p}_i\}_{i=1}^K$ ;
4 while not converged do
5   | compute mass centroids  $\mathbf{c}_i$  for  $\{V_i\}_{i=1}^K$ ;
6   | update  $\{\mathbf{p}_i\}_{i=1}^K \leftarrow \{\mathbf{c}_i\}_{i=1}^K$ ;
7   | construct new Voronoi tessellation;
8 end

```

Supplementary Note 4. Image Reconstruction

In this note, we explain the details of the image reconstruction and provide a comparison against very recent phase-type lensless cameras that share the most similar inspiration with ours, DiffuserCam⁶ and PhlatCam⁷. We compare the imaging performance here in Fig. S1. To ensure a fair comparison, all the simulations are performed with the same condition. We assume the sensor pixel pitch is $4 \mu\text{m}$, and the resolution of the phase element is $1 \mu\text{m}$, which provides a good sampling rate between the two. The sensor pixels are 256×256 , and Voronoi-Fresnel phase is

1024×1024 . The distance between the optical element and the sensor is 2 mm. The PSFs for the Voronoi-Fresnel design and the PhlatCam design are obtained through a full spectrum simulation, from 400 nm to 700 nm with an interval of 10 nm (totally 31 spectral bands). We are not able to simulate a diffuser PSF, so we adopt the closest PSF from DiffuserCam⁶, and assume the intensities are the same for the three color channels. We use multispectral image data⁸ for the full spectrum simulation. An example raw data with their respective PSFs are shown in Fig. S1a. Owing to the contrast, sparsity and distribution of the PSF patterns, the raw data from our lensless camera is more structured than flattened in the other two cases. The corresponding reconstructed images are shown in Fig. S1b. We evaluate the performance by Peak Signal to Noise Ratio (PSNR) and Structural Similarity Index (SSIM) in Fig. S1c. Larger values indicate better performance. As a reference, the ground-truth image is shown in Fig. S1d. The ground-truth color image is generated by assuming the spectral PSFs are Dirac delta functions.

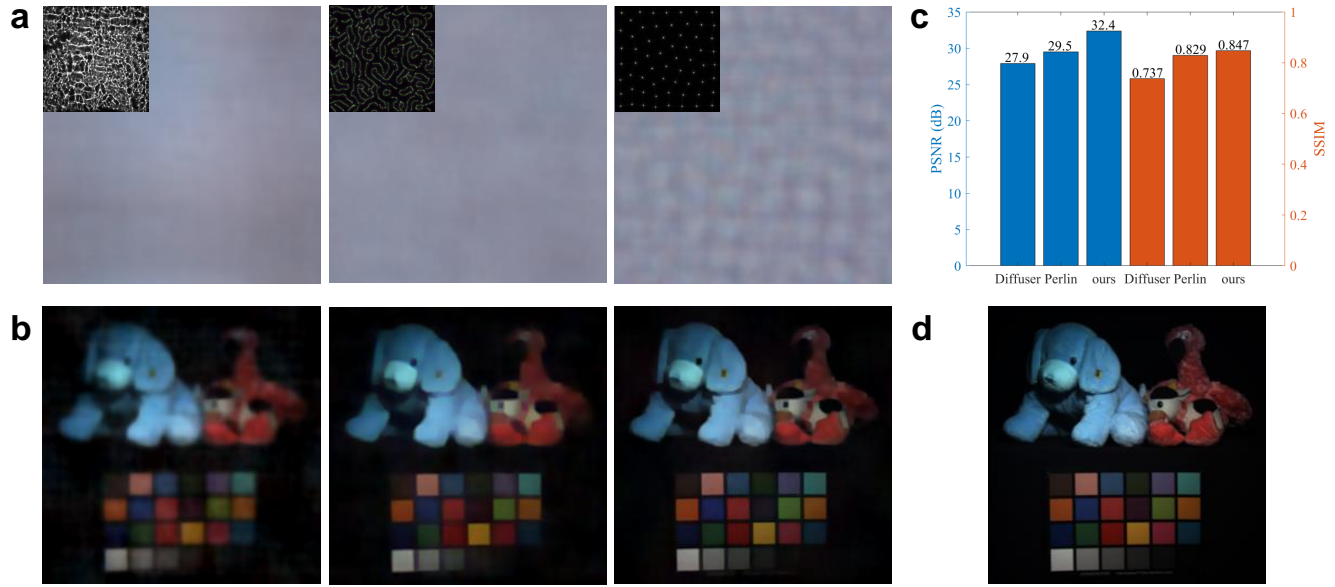


Fig. S1. Comparison of image reconstruction results. **a** Raw sensor data for the DiffuserCam (left) with diffuser PSF, PhlatCam (middle) with Perlin PSF, and the proposed Voronoi-Fresnel camera (right). The corresponding PSFs are shown in the top-left corner. **b** Image reconstruction results from **a**. **c** PSNR and SSIM results for the three methods. **d** Reference ground-truth color image.

Supplementary Note 5. Prototype

The prototype Voronoi-Fresnel phase is designed at 550 nm for 2π modulation. Considering the fabrication resolution and sensor pixel size, we fix the upsampling ratio of $3\times$ for the optical element, i.e., $1.15 \mu\text{m}$, which is well controlled by our fabrication method. The sensor has 1440×1080 pixels, and the Voronoi-Fresnel phase has 4320×3240 pixels. The optimized full-area phase profile is shown in Fig. S2a. Our sensor has a field-of-view of $\pm 20^\circ$ in the horizontal direction and $\pm 15^\circ$ in the vertical direction, so we design an aperture (Fig. S2b) that excludes the cells outside of the field-of-view. The optimal number of Voronoi-Fresnel cells from the optimization is 594, as shown in Fig. S2c after the parameter sweep step. The effective cells within the field-of-view is 424, which is about 71.4% of the total number.

The final presentation of the image requires some necessary pre-processing and post-processing for better image presentation. We first demosaic the raw sensor data into color image data according to the sensor Bayer layout. Before image reconstruction, we normalize the blurred data by its norm in each color channel. For all the experimental results, the weights are all set to $\mu = 1e^{-7}$, and $\rho = 1e^{-5}$. In the post-processing, we use a simple gray world algorithm in MATLAB (chromadapt) for automatic white balancing in the linear color space. The illuminant is estimated by excluding 10 percentile of pixels. Finally gamma correction ($\gamma = 1.25$) is applied.

We present additional characteristic test results for the prototype in Fig. S3. First, we evaluate the geometry distortion using a checkerboard target. As shown in Fig. S3a, the geometry is restored very well across the $\pm 20^\circ \times \pm 15^\circ$ field-of-view. On the border regions, there are residual chromatic artifacts, however. This may arise

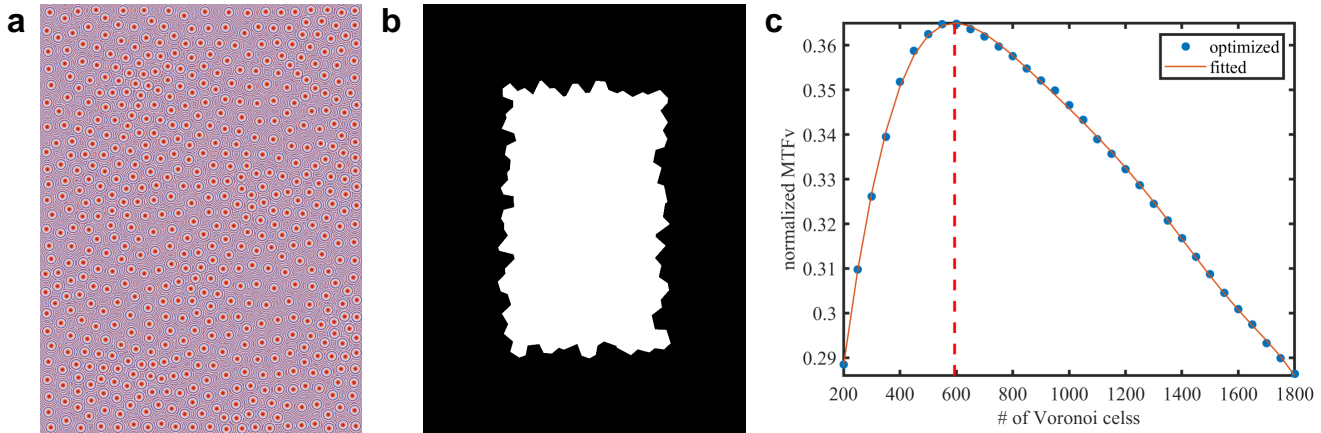


Fig. S2. Design of the prototype Voronoi-Fresnel lensless camera. **a** Optimized full-area phase profile. **b** An aperture to maintain the PSF shift-invariance within $\pm 20^\circ$ field-of-view. **c** Best number of Voronoi-Fresnel cells in the parameter sweep step. The optimal number of cells is 594 without the aperture. Effective cells after applying the aperture is 424.

from two factors. One is the off-axis aberrations of the base Fresnel phase, and the other is the difference in PSFs from on-axis to off-axis leading to the drop in reconstruction quality. Second, we evaluate the color fidelity using a color checker target. Despite the residual color artifacts in the border regions, the overall color fidelity is retrieved from the raw data. Potential improvement could be a more advanced white balancing algorithm other than the simple gray world algorithm used here. Last, we evaluate the spatial resolution variation using a Siemens star target. A uniform spatial resolution change is observed from the reconstructed image, demonstrating again that the MTF optimization is effective with uniform response.

Additionally, we present more example results in Fig. S4. Again, the results in Fig. S4a and S4b are captured from self-illuminating images displayed on a monitor, and Fig. S4c and S4d are real objects with ambient illumination. Details in the objects are well preserved after reconstruction in both cases.

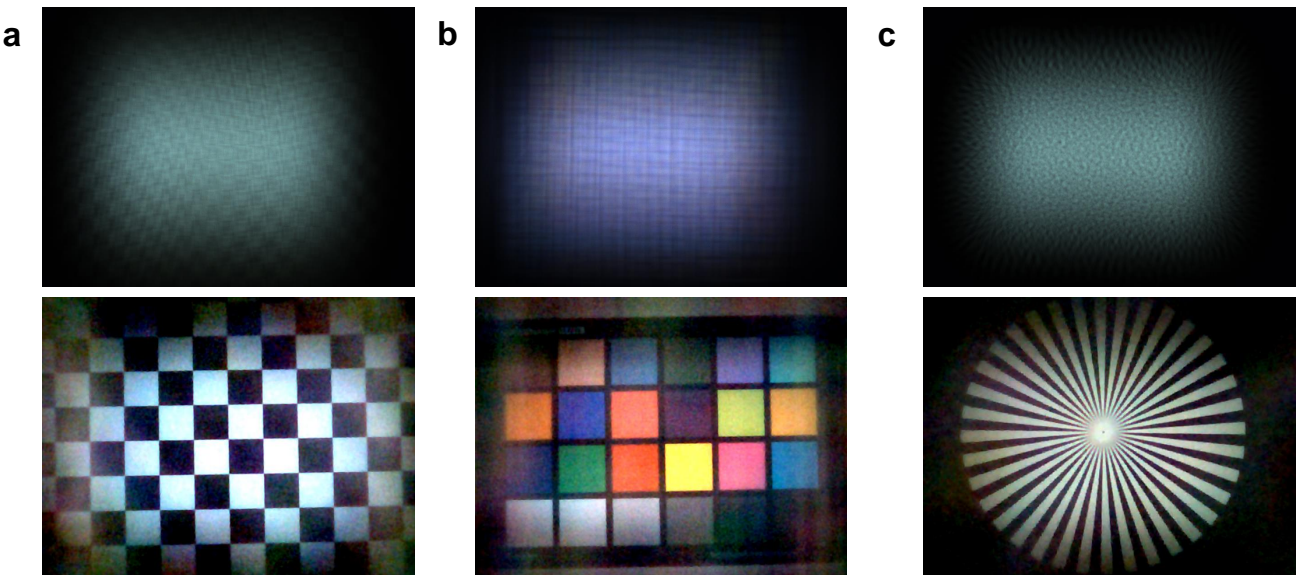


Fig. S3. Prototype characteristic test results. The reconstruction of a checkerboard image in **a** shows little geometry distortion. The color checker in **b** indicates good color recovery, although residual color artifacts exist in the image border. **c** A Siemens star image shows uniform resolution preservation in all directions.

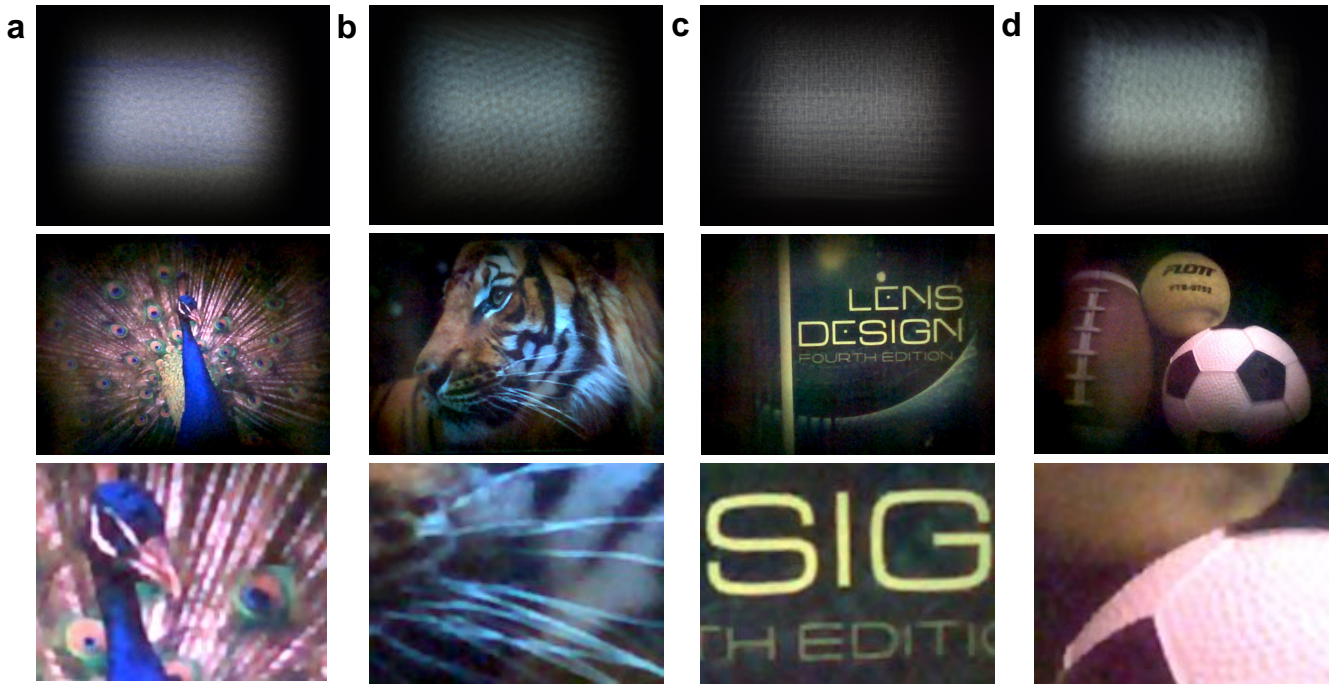


Fig. S4. Additional prototype results. **a** and **b** show results for self-illuminating images displayed on a computer monitor. **c** and **d** show results for real objects with ambient illumination. Top row are the captured raw data; middle row are reconstructed images; and bottom row are zoom-in details.

References

1. Yan, D.-M., Guo, J.-W., Wang, B., Zhang, X.-P. & Wonka, P. A survey of blue-noise sampling and its applications. *J Comput. Sci. Technol.* **30**, 439–452 (2015).
2. De Goes, F., Breeden, K., Ostromoukhov, V. & Desbrun, M. Blue noise through optimal transport. *ACM Trans. Graph.* **31**, 1–11 (2012).
3. Du, Q., Faber, V. & Gunzburger, M. Centroidal Voronoi tessellations: Applications and algorithms. *SIAM Rev. Soc. Ind. Appl. Math.* **41**, 637–676 (1999).
4. Yan, D.-M., Wang, K., Lévy, B. & Alonso, L. Computing 2D periodic centroidal voronoi tessellation. In *2011 Eighth International Symposium on Voronoi Diagrams in Science and Engineering*, 177–184 (IEEE, 2011).
5. Lloyd, S. Least squares quantization in PCM. *IEEE Trans. Inf. Theory* **28**, 129–137 (1982).
6. Antipa, N. *et al.* DiffuserCam: lensless single-exposure 3D imaging. *Optica* **5**, 1–9 (2018).
7. Boominathan, V., Adams, J., Robinson, J. & Veeraraghavan, A. Phlatcam: Designed phase-mask based thin lensless camera. *IEEE Trans. Pattern Anal. Mach. Intell.* (2020).
8. Yasuma, F., Mitsunaga, T., Iso, D. & Nayar, S. Generalized Assorted Pixel Camera: Post-Capture Control of Resolution, Dynamic Range and Spectrum. Tech. Rep. (2008).